AALBORG UNIVERSITY

Nonlinear photocurrents in two-dimensional systems based on graphene and boron nitride

Hipolito, F. ; Pedersen, Thomas Garm; Peria, V.M.

Link to publication from Aalborg University

Nonlinear photocurrents in two-dimensional systems based on graphene and boron nitride

F. Hipolito,[1,2] Thomas G. Pedersen,[3,4] and Vitor M. Pereira[5,2,*]

[1]*NUS Graduate School for Integrative Sciences and Engineering, Centre for Life Sciences, Singapore 117456*
[2]*Centre for Advanced 2D Materials, National University of Singapore, 6 Science Drive 2, Singapore 117546*
[3]*Department of Physics and Nanotechnology, Aalborg University, DK-9220 Aalborg Øst, Denmark*
[4]*Center for Nanostructured Graphene (CNG), DK-9220 Aalborg Øst, Denmark*
[5]*Department of Physics, National University of Singapore, 2 Science Drive 3, Singapore 117542*

The dc photoelectrical currents can be generated purely as a nonlinear effect in uniform media lacking inversion symmetry without the need for a material junction or bias voltages to drive it, in what is termed photogalvanic effect. These currents are strongly dependent on the polarization state of the radiation, as well as on topological properties of the underlying Fermi surface such as its Berry curvature. In order to study the intrinsic photogalvanic response of gapped graphene, biased bilayer graphene (BBG), and hexagonal boron nitride (hBN), we compute the nonlinear current using a perturbative expansion of the density matrix. This allows a microscopic description of the quadratic response to an electromagnetic field in these materials, which we analyze as a function of temperature and electron density. We find that the intrinsic response is robust across these systems and allows for currents in the range of pA cm/W to nA cm/W. At the independent-particle level, the response of hBN-based structures is significant only in the ultraviolet due to their sizable band gap. However, when Coulomb interactions are accounted for by explicit solution of the Bethe-Salpeter equation, we find that the photoconductivity is strongly modified by transitions involving exciton levels in the gap region, whose spectral weight dominates in the overall frequency range. Biased bilayers and gapped monolayers of graphene have a strong photoconductivity in the visible and infrared window, allowing for photocurrent densities of several nA cm/W. We further show that the richer electronic dispersion of BBG at low energies and the ability to change its band gap on demand allows a higher tunability of the photocurrent, including not only its magnitude but also, and significantly, its polarity.

I. INTRODUCTION

Nonlinear photocurrents consist of dc electric currents induced in a material by nonlinear interaction with an external electromagnetic field. This is frequently termed *photogalvanic* or *optical rectification* effect [1,2]. It belongs to a vast class of processes arising from the nonlinear response of matter to light fields, such as higher harmonic generation, sum/difference frequency generation, optical rectification, parametric oscillation, two-photon absorption, or stimulated Raman scattering. These processes have a broad range of applications, from nonlinear optical microscopy, optical switching, tunable high-frequency lasers, surface analysis with nonlinear optics, to parametric down conversion for generation of entangled photons [3–6] and photocurrents [1,6]. The photogalvanic effect is particularly interesting for optoelectronic applications as it opens the door for light-induced injection and steering of electric or spin currents [2] without electrical contacts or the need of electric fields to separate photoexcited electron-hole pairs, as commonly happens in most applications of photogenerated currents.

In metallic structures, the nonlinear response to external fields is frequently dominated by surface states as a result of the large absorption in metals. This is both interesting and convenient in bulk crystals with inversion symmetry because elastic even-order interactions with electromagnetic fields are suppressed by symmetry in the bulk, but might be possible at the surface where the inversion symmetry is broken [5,7].

The wealth of strictly two-dimensional systems that emerged in the wake of the success of graphene, with a range of different intrinsic optoelectronic properties that continues to grow, provide a particularly fertile setting to explore nonlinear optical properties. Two of their important characteristics in this context are the intrinsically low absorption as light traverses only one or a few atomic layers, and the ease to fabricate planar heterostructures based on combining different functionalities that are important for photoelectric and photogalvanic devices. Moreover, in many of them the electronic density and/or gap can be tuned externally by field effect [8,9] or electrolytic gating [10], thereby allowing control over two key parameters that determine the optical response.

In this paper, we analyze the characteristics of the second-order electrical conductivity tensor with a focus on the intrinsic photoconductivity of graphene-based systems and boron nitride using a perturbative expansion of the density matrix. We start with a brief analysis of symmetry, followed by an overview of the formalism proposed in Ref. [11] to compute the relevant response functions. In the main sections, we analyze in detail the features of the photoconductivity in monolayers of "gapped graphene," of which the canonical example is hBN (hexagonal boron nitride), as well as their bilayer counterparts which can display a richer response when the interlayer bias and chemical potential are independently controlled. The photogalvanic reponse is a second-order nonlinear effect and, therefore, requires broken inversion symmetry in the dipole limit. We systematically investigate the influence of stacking sequence on the inversion symmetry of various bilayer structures. It has previously been established that the second-order nonlinear optical response, in the form

---

*Corresponding author: vpereira@nus.edu.sg

of second harmonic generation, in bilayer graphene is very large [12]. Moreover, the response is highly tunable by external gating or variations in doping level. We find that similar conclusions hold for the photogalvanic response.

In the last section, we address the role of excitons in the photoconductivity of these two-dimensional insulators, and establish that, similarly to the large renormalization that they cause in the linear optical conductivity, the excitonic response is crucial for an accurate characterization of the quadratic response. The important role of excitons in second harmonic generation from two-dimensional materials has previously been demonstrated for MoS_2 and hBN [13,14]. Hence, in the last part of this paper, we apply the excitonic intraband formalism developed in Ref. [14] to include Coulomb interactions in the nonlinear photoconductivity of hBN. In this manner, we show that excitons lead to a large red-shift of the response as well as a renormalization of the spectrum above the band gap.

II. SYMMETRY CONSIDERATIONS

The essence of response theory applied to photocurrent generation is that, when an electromagnetic wave with electric field

$$\mathbf{E}(t) = \frac{1}{2} \sum_{\omega_n} E_{\omega_n}^{\alpha} e^{-i\omega_n t}\, \hat{\mathbf{e}}_{\alpha} \tag{1}$$

impinges on an electronic system, the induced current density can be, quite generically, expressed as a sum of contributions proportional to increasing powers of the field magnitude

$$J_{\lambda}(t) = \sum_{N=1}^{\infty} \sum_{\{\omega_k\}} \sigma_{\lambda\alpha\ldots\beta}^{(N)}(\omega_1,\ldots,\omega_N) \frac{E_{\omega_1}^{\alpha}\ldots E_{\omega_N}^{\beta}}{e^{i(\omega_1+\cdots+\omega_N)}}. \tag{2}$$

This defines the Nth-order frequency-dependent conductivity, a tensor of rank $N+1$ that determines the Cartesian component λ of the current $J_{\lambda}(t)$ as a function of time. A perennial question in this context is to determine $\sigma_{\lambda\alpha\ldots\beta}^{(N)}(\omega_1,\ldots,\omega_N)$ at a given order from the microscopic details of the target system (symmetry, electronic structure, interactions, etc.).

The dc photocurrent arising in the intrinsic photogalvanic effect results from the existence of a nonzero quadratic response $\sigma_{dc}^{(2)}(\omega) \equiv \sigma_{\lambda\alpha\beta}^{(2)}(\omega,-\omega)$ in systems that fulfill certain symmetry criteria. Foremost is the fact that, being an odd-rank tensor, it can only be sustained in the absence of inversion symmetry. In addition to this, the most basic threefold symmetry common to all honeycomb-based lattices considerably reduces the nonzero independent components of $\sigma^{(2)}$. Under the C_3 point-group symmetry, we have only two independent in-plane components, say $\sigma_{111}^{(2)}$ and $\sigma_{222}^{(2)}$, as well as the constraints $\sigma_{211}^{(2)} = \sigma_{121}^{(2)} = \sigma_{112}^{(2)} = -\sigma_{222}^{(2)}, \sigma_{122}^{(2)} = \sigma_{212}^{(2)} = \sigma_{221}^{(2)} = -\sigma_{111}^{(2)}$. In Table I, we identify the symmetry and nonvanishing components of rank-3 tensors for monolayers and bilayers of graphene and hBN that are appropriate for the target systems in this paper. It contains the relevant space (SG) and point groups (PG) for the lattices under consideration and highlights the presence or absence of inversion symmetry in each case [7,15].

Among the cases selected to analyze in detail here, the restrictions imposed by lattice symmetry are most stringent in graphene, where both free-standing monolayer and AB bilayers have inversion symmetry. However, second-order

TABLE I. Summary of basic symmetry properties for monolayers and bilayers of graphene and hBN. SG: space group, PG: point group, i: inversion. The last column indicates the independent, nonvanishing elements of a rank-3 tensor. The labeling of stacking order in hBN follows Ref. [16], where AA indicates two pairs of vertically aligned atoms in the unit cell, while only one pair is vertically aligned in the AB stacking.

Material	Stacking	SG	PG	i	$t_{ijk} \neq 0$
Graphene	SL	$P6/mmm$	$6/mmm \equiv D_{6h}$	yes	none
	AB	$P\bar{3}m1$	$\bar{3}m \equiv D_{3d}$	yes	none
(Biased)	AB	$P3m1$	$3m \equiv C_{3v}$	no	t_{222}
hBN	SL	$P\bar{6}m2$	$\bar{6}m2 \equiv D_{3h}$	no	t_{222}
	AA	$P\bar{6}m2$	$\bar{6}m2 \equiv D_{3h}$	no	t_{222}
	AA$'$	$P\bar{3}m1$	$\bar{3}2/m \equiv D_{3d}$	yes	none
	AB	$P3m1$	$3m \equiv C_{3v}$	no	t_{222}
	A$'$B	$P\bar{3}m1$	$\bar{3}2/m \equiv D_{3d}$	yes	none
	AB$'$	$P\bar{3}m1$	$\bar{3}2/m \equiv D_{3d}$	yes	none

response is possible in biased AB graphene bilayers because the potential difference between the two layers naturally breaks that symmetry [12]. In contrast, due to the presence of two distinct elements in the unit cell, an hBN monolayer does not have an inversion center and, consequently, its quadratic response can be finite. In addition, the stacking order plays an important role in hBN bilayers since a majority of possible stackings results in inversion-symmetric lattices (namely, AA$'$, A$'$B, and AB$'$). In the remainder of this paper, we will compute and analyze the intrinsic photoconductivity of the systems listed in the table whose response is not suppressed by symmetry.

III. CALCULATION OF NONLINEAR RESPONSE FUNCTIONS

We shall be interested in the interaction of the electronic system in a crystal with light, for which we can neglect the position dependence of the electromagnetic field in a first (dipole) approximation, and write the total Hamiltonian of the system as

$$\hat{H} = \hat{H}_0 + \hat{V}(t), \quad \hat{V}(t) = e\,\hat{\mathbf{r}} \cdot \mathbf{E}(t). \tag{3}$$

Here, $\hat{H}_0$ represents the Hamiltonian of the electrons in the periodic crystal and $\mathbf{E}(t)$ the explicitly time-dependent external field and $e > 0$ is the elementary charge. The field is taken to be monochromatic and parametrized as in Eq. (1). The eigenvalues of the unperturbed Hamiltonian $\hat{H}_0$ define the band energies $\epsilon_n(\mathbf{k})$, and its eigenstates $|n\mathbf{k}\rangle$ are the corresponding Bloch waves. In the derivations below, electronic interactions are neglected and, hence, collective effects arise simply on account of the Fermi-Dirac statistics. In the last section, however, we investigate the effect of Coulomb interactions on the excited electronic states, i.e., excitons. These effects are studied only for the simple case of monolayer hBN, though.

A. Perturbative expansion of the density matrix

The time evolution of a system governed by the Hamiltonian (3) is entirely determined if one computes the

time-dependent density operator

$$\hat{\rho}(t) \equiv \sum_{mn} \rho_{mn}(t)|m\rangle\langle n|, \tag{4}$$

that obeys the dynamical (quantum Liouville) equation $i\hbar\,\partial\hat{\rho}/\partial t = [\hat{H},\hat{\rho}]$ or, more explicitly,

$$\frac{\partial \rho_{mn}}{\partial t} = \frac{\epsilon_{mn}\,\rho_{mn}}{i\hbar} + \sum_{l} \frac{V_{ml}\,\rho_{ln} - \rho_{ml}\,V_{ln}}{i\hbar}. \tag{5}$$

Knowledge of $\hat{\rho}(t)$ permits one to readily quantify and characterize the electric current density in terms of the polarization and intensity of the field $\mathbf{E}(t)$. The current density is given in terms of the single-particle velocity operator

$$\hat{\mathbf{v}} \equiv \frac{i}{\hbar}[\hat{H}, \hat{\mathbf{r}}] \tag{6}$$

by

$$\mathbf{J}(t) \equiv \mathrm{Tr}\,[\hat{\rho}(t)\,\hat{\mathbf{j}}] = -\frac{ge}{\Omega} \sum_{\mathbf{k}} \sum_{mn} \boldsymbol{v}_{nm}\,\rho_{mn}(t), \tag{7}$$

where $g = 2$ accounts for the spin degeneracy and Ω is the D-dimensional volume of the system.

The formal integration of (5) is facilitated in the interaction picture with respect to the external perturbation, and leads to the conventional perturbative expansion of the density operator in powers of the perturbation $\hat{V}(t)$ [17]. In a crystal, however, such straightforward expansion cannot be directly used for the perturbation defined in (3) because it involves matrix elements of the position between Bloch states such as $\langle m\mathbf{k}|\hat{\mathbf{r}}|n\mathbf{k}'\rangle$, which are notably ill defined [18]. The integration of Eq. (5) thus requires a more careful treatment of these matrix elements. Moreover, the potential alternative of effecting a gauge transformation to describe the external field in the minimal coupling scheme $\mathbf{p} \to \mathbf{p} + e\mathbf{A}$ is plagued by its own difficulties in the nonlinear response functions it generates, most notably the appearance of nonphysical divergences in the dc limit of an insulator at zero temperature [19]. To navigate these difficulties, we follow the systematic approach proposed in Ref. [11] to handle the external field perturbation as expressed in Eq. (3). In order to provide here a self-contained account of our calculations, we briefly review the key aspects of that approach.

An important step is to express matrix elements of the position operator between Bloch states as [18]

$$\langle m\mathbf{k}|\hat{\mathbf{r}}|n\mathbf{k}'\rangle = i\delta_{mn}\nabla_{\mathbf{k}}\delta_{\mathbf{k},\mathbf{k}'} + \delta_{\mathbf{k},\mathbf{k}'}\,\mathcal{A}_{mn}(\mathbf{k}), \tag{8}$$

where $\mathcal{A}_{mn}(\mathbf{k})$ is the so-called Berry connection [11,20,21] and

$$\delta_{\mathbf{k},\mathbf{k}'} \equiv \frac{\Omega_C}{\Omega} \sum_{\mathbf{R}} e^{i(\mathbf{k}-\mathbf{k}')\cdot\mathbf{R}} \tag{9}$$

is the Kronecker delta with Ω_C representing the volume of the unit cell. We normalize the Bloch states in the finite volume Ω as

$$\psi_{n\mathbf{k}}(\mathbf{r}) \equiv \langle \mathbf{r}|n\mathbf{k}\rangle = \frac{e^{i\mathbf{k}\cdot\mathbf{r}}}{\sqrt{\Omega}} u_{n\mathbf{k}}(\mathbf{r}), \tag{10}$$

with $u_{n\mathbf{k}}(\mathbf{r})$ a cell-periodic function. The Berry connection then has the explicit form

$$\mathcal{A}_{mn} \equiv \frac{i}{\Omega_c} \int_{\Omega_C} d\mathbf{r}\, u^*_{m\mathbf{k}}(\mathbf{r})\nabla_{\mathbf{k}} u_{n\mathbf{k}}(\mathbf{r}). \tag{11}$$

For brevity, we will frequently omit the explicit $\mathbf{k}$ dependence in $\mathcal{A}_{mn}$, ρ_{mn} and other quantities when there is no risk of confusion. Equation (8) suggests a natural identification of two types of matrix elements, interband and intraband, respectively given by

$$\mathbf{r}^{(e)}_{mn} \equiv \langle m\,\mathbf{k}|\hat{\mathbf{r}}^{(e)}|n\,\mathbf{k}'\rangle = \bar{\delta}_{mn}\,\delta_{\mathbf{k},\mathbf{k}'}\mathcal{A}_{mn}, \tag{12a}$$

$$\mathbf{r}^{(i)}_{mn} \equiv \delta_{mn}[\delta_{\mathbf{k},\mathbf{k}'}\mathcal{A}_{mn} + i\nabla_{\mathbf{k}}\delta_{\mathbf{k},\mathbf{k}'}]. \tag{12b}$$

In this expression, δ_{mn} is the usual Kronecker delta and $\bar{\delta}_{mn} \equiv 1 - \delta_{mn}$. This allows a decomposition of the position operator into a purely interband component and another purely intraband $\hat{\mathbf{r}} = \hat{\mathbf{r}}^{(i)} + \hat{\mathbf{r}}^{(e)}$, with

$$\hat{\mathbf{r}}^{(e)} \equiv \sum_{\mathbf{k}\mathbf{k}'} \sum_{m\neq n} \mathbf{r}^{(e)}_{mn}\,|m\mathbf{k}\rangle\langle n\mathbf{k}'|, \tag{13}$$

$$\hat{\mathbf{r}}^{(i)} \equiv \sum_{\mathbf{k}\mathbf{k}'} \sum_{m} \mathbf{r}^{(i)}_{mm}\,|m\mathbf{k}\rangle\langle m\mathbf{k}'|. \tag{14}$$

With these definitions, Eq. (5) can be recast as [11]

$$i\hbar\frac{\partial \rho_{mn}}{\partial t} = \hbar\omega_{mn}\,\rho_{mn} + ie\,(\rho_{mn})_{;\mathbf{k}} \cdot \mathbf{E}(t)$$
$$+ e \sum_{l}[\bar{\delta}_{ml}\mathcal{A}_{ml}\,\rho_{ln} - \rho_{ml}\bar{\delta}_{ln}\mathcal{A}_{ln}] \cdot \mathbf{E}(t), \tag{15}$$

where $\hbar\omega_{mn}(\mathbf{k}) \equiv \epsilon_m(\mathbf{k}) - \epsilon_n(\mathbf{k})$ and the second term contains the generalized (gauge-invariant) gradient [11]

$$(\rho_{mn})_{;\mathbf{k}} \equiv \nabla_{\mathbf{k}}\rho_{mn} - i\rho_{mn}(\mathcal{A}_{mm} - \mathcal{A}_{nn}). \tag{16}$$

The purpose of writing Eq. (5) as (15) is that, now, all the matrix elements appearing in (15) are well defined and nonsingular, which would not be the case if we had generated an equivalent expansion in terms of matrix elements $\mathbf{r}_{mn}$ directly from (5).

Equation (15) can be straightforwardly integrated recursively yielding a series in increasing powers of the electric field

$$\rho_{mn}(t) = \sum_{N=0}^{\infty} \rho^{(N)}_{mn}(t). \tag{17}$$

Each term $\rho^{(N)}_{mn}(t)$ is associated with the $(N-1)$th-order response function. Since we are ultimately interested in the electrical currents induced by the external radiation field, we will compute the nonlinear conductivity which is the natural response function for this case. In the absence of the light field, the system is in equilibrium and its effective single-particle density matrix reduces to $\rho_{mn}(t)|_{\mathbf{E}=0} = \rho^{(0)}_{mn} = \delta_{mn}f[\epsilon_m(\mathbf{k})]$, a simple Fermi-Dirac distribution. This unperturbed density matrix begins the iterative solution of Eq. (15) which is then straightforward and we obtain, in first order in the electric field,

$$\frac{\rho^{(1)}_{mn}(t)}{2\hbar/e} = \sum_{\omega_1}\left[\bar{\delta}_{mn}\mathcal{A}^\alpha_{mn}f_{nm} - i\delta_{mn}\frac{\partial f_n}{\partial k_\alpha}\right]\frac{E^\alpha_{\omega_1}e^{-i(\omega_1+i\eta)t}}{\omega_1 - \omega_{mn} + i\eta}, \tag{18a}$$

where we introduced $f_n \equiv f[\epsilon_n(\mathbf{k})]$, $f_{nm} \equiv f[\epsilon_n(\mathbf{k})] - f[\epsilon_m(\mathbf{k})]$, and the frequency summation $\sum_{\omega_1}$ should be interpreted as including the two possible Fourier components, i.e., $\sum_{\omega_1} g(\omega_1) \equiv g(-\omega_1) + g(\omega_1)$. Also, $i\eta$ with η a positive infinitesimal is added to each frequency to ensure adiabatic turn-on of the field. However, to improve numerical stability and account for broadening in realistic spectra, we will keep η finite but small throughout. In addition, in (18a) and henceforth, Greek superscripts denote Cartesian components and are implicitly summed over when they appear repeated. The second-order contribution to the density matrix reads as

$$
\rho_{mn}^{(2)}(t) = \frac{e^2}{4\hbar^2} \sum_{\omega_2,\omega_1} \sum_{l} \frac{E_{\omega_2}^\beta E_{\omega_2}^\alpha e^{-i(\omega_2+\omega_1+2i\eta)t}}{\omega_2 + \omega_1 - \omega_{mn} + 2i\eta}
$$
$$
\times \left[\bar{\delta}_{lm}\bar{\delta}_{ln} \left(\frac{\mathcal{A}_{ml}^\beta \mathcal{A}_{ln}^\alpha f_{nl}}{\omega_1 - \omega_{ln} + i\eta} - \frac{f_{lm}\mathcal{A}_{ml}^\alpha \mathcal{A}_{ln}^\beta}{\omega_1 - \omega_{ml} + i\eta} \right) \right.
$$
$$
- \frac{\delta_{lm}\delta_{mn}}{\omega_1 + i\eta} \frac{\partial^2 f_n}{\partial k_\beta \partial k_\alpha} - i\, \delta_{lm}\bar{\delta}_{mn} \frac{\mathcal{A}_{mn}}{\omega_1 + i\eta} \frac{\partial f_n}{\partial k_\alpha}
$$
$$
\left. - i\, \delta_{lm}\bar{\delta}_{mn} \left(\frac{\mathcal{A}_{mn}^\alpha f_{nm}}{\omega_1 - \omega_{mn} + i\eta} \right)_{;k_\beta} \right], \tag{18b}
$$

where the generalized derivative introduced in Eq. (16) appears explicitly in the last term.

B. Linear and quadratic response functions

The current response at any desired order is obtained by substituting the perturbative expansion (17) in Eq. (7):

$$
\mathbf{J}(t) = \sum_{N=0}^{\infty} \hat{\mathbf{J}}^{(N)}(t), \tag{19}
$$

where

$$
\hat{\mathbf{J}}^{(N)}(t) \equiv -\frac{ge}{\Omega} \sum_{\mathbf{k}} \sum_{mn} \boldsymbol{v}_{nm}\, \rho_{mn}^{(N)}(t). \tag{20}
$$

According to the earlier definition in Eq. (2),

$$
J_\lambda^{(N)}(t) = \sum_{\{\omega_k\}} \sigma_{\lambda\alpha\ldots\beta}^{(N)}(\omega_1,\ldots,\omega_N) \frac{E_{\omega_1}^\alpha \ldots E_{\omega_N}^\beta}{e^{-i(\omega_1+\cdots+\omega_N)t}}, \tag{21}
$$

which defines the Nth-order optical conductivity $\sigma_{\lambda\alpha\ldots\beta}^{(N)}(\omega_1,\ldots,\omega_N)$. In this expression, $\Sigma_{\{\omega_k\}}$ means a summation that runs over all $\omega_1,\ldots,\omega_N$, and each ω_k takes all the values that define the harmonic content of the external field. In the case of a single source of monochromatic light as in (1), we have simply $\omega_k = \pm\omega$. Equation (21) transparently shows that, in quadratic and higher orders, the time dependence of the response is richer than that of the external field, with the characteristic appearance of up to N higher-order harmonics of the input frequency. In particular, in second order we see that it is possible to induce a dc contribution (constant in time) to $J_\lambda^{(N)}(t)$ that is determined by $\sigma_{\lambda\alpha\beta}^{(2)}(\omega,-\omega)$. *This particular response function, the photoconductivity, is our main focus in this paper.*

As a preliminary illustration, one obtains the linear optical conductivity by directly combining the results in Eq. (18) with the definitions above:

$$
\sigma_{\lambda\alpha}^{(1)}(\omega) = \frac{2ig\hbar^2 \sigma_1}{\Omega} \sum_{\mathbf{k}} \sum_{mn} \sum_{\omega} \frac{v_{nm}^\lambda}{\hbar\omega - \epsilon_{mn} + i\Gamma}
$$
$$
\times \left[-\frac{\delta_{mn}}{\hbar} \frac{\partial f_n}{\partial k_\alpha} + \bar{\delta}_{mn} \frac{v_{mn}^\alpha f_{nm}}{\epsilon_{mn}} \right], \tag{22}
$$

with $\sigma_1 \equiv e^2/4\hbar$, $\omega_{mn} \equiv \epsilon_{mn}/\hbar$, and $\eta \equiv \Gamma/\hbar$. We have written $\sigma_{\lambda\alpha}^{(1)}(\omega)$ explicitly in terms of the matrix elements of the velocity operator v_{mn} using the relation $\mathcal{A}_{mn}^\alpha = i\hbar v_{mn}^\alpha/\epsilon_{mn}$ that follows from Eqs. (6) and (12) when $m \neq n$. Note that, in this form, the two terms that make up the result above directly, and individually, reflect the interband ($\propto\delta_{mn}$) and intraband ($\propto\bar{\delta}_{mn}$) contributions to the overall optical conductivity. For example, the Drude component $\propto(\hbar\omega_1 + i\Gamma)^{-1}$ can be read from the first term in (22) due to the constraint $m = n$. In fact, one can readily see that

$$
\mathrm{Re}\big[\sigma_{\alpha\alpha}^{(1),\mathrm{intra}}(\omega, T=0)\big] = D^\alpha(\mu)\, \delta(\omega), \tag{23}
$$

where the Drude weight is $D^\alpha(\mu) \equiv 2\pi\hbar\sigma_1 N(\mu) \sum_m \langle |v_{mm}^\alpha(\mathbf{k})|^2 \rangle_\mu$, $N(\mu)$ is the density of states (DOS) at the Fermi level, and $\langle\ldots\rangle_\mu$ denotes an average over the Fermi surface [22]. This component is zero in the presence of a band gap for a clean system (as happens in most of the situations we consider throughout this paper) as long as the chemical potential remains in the gapped region and the temperature is low. In such cases, that include the peculiar situation of undoped graphene, the linear conductivity is uniquely determined by the interband component [22–25]. Several examples are shown in Fig. 1.

The clear distinction between interband and intraband terms in the final expressions for the conductivity is a direct result of the earlier decomposition of the position matrix elements (12), and propagates to higher orders [11]. In particular, the quadratic conductivity can be decomposed into four distinct
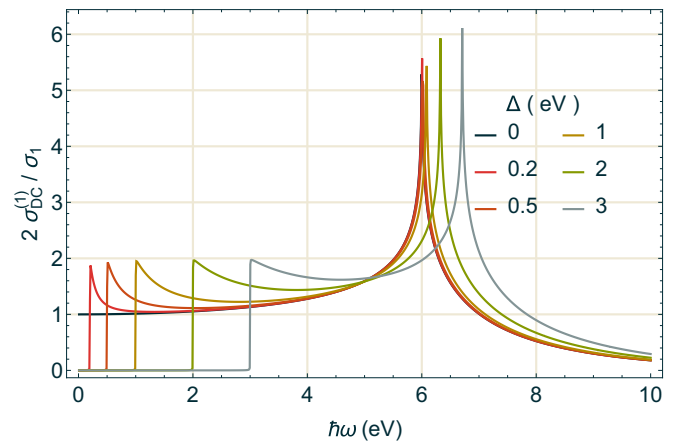

FIG. 1. Diagonal components of $\mathrm{Re}\,\sigma_{\alpha\beta}^{(1)}(\omega)$ in gapped graphene. The factor of 2 in the vertical axis stems from the definitions (1) and (21), and $\sigma_1 \equiv e^2/4\hbar$. We used the TB model (28) [$\gamma_0 = 3$ eV, $\Gamma = 0.5$ meV, $\mu = 0$ eV].

contributions:

$$\sigma_{\lambda\alpha\beta}^{(2)}(\omega_1,\omega_2) = \sigma_{\lambda\alpha\beta}^{(2,ee)} + \sigma_{\lambda\alpha\beta}^{(2,ie)} + \sigma_{\lambda\alpha\beta}^{(2,ei)} + \sigma_{\lambda\alpha\beta}^{(2,ii)}, \quad (24)$$

where

$$\sigma_{\lambda\alpha\beta}^{(2,ee)}(\omega_1,\omega_2)$$

$$\equiv \sigma_2 g \frac{\hbar^3 \gamma_0}{\Omega a} \sum_{\mathbf{k}} \sum_{lmn} \frac{\bar{\delta}_{lm}\bar{\delta}_{ln}\, v_{nm}^{\lambda}\,/\,\epsilon_{ml}\epsilon_{ln}}{\hbar(\omega_2+\omega_1) - \epsilon_{mn} + 2i\Gamma}$$

$$\times \left(\frac{v_{ml}^{\beta} v_{nm}^{\alpha} f_{nl}}{\hbar\omega_1 - \epsilon_{ln} + i\Gamma} - \frac{f_{lm} v_{ml}^{\alpha} v_{ln}^{\beta}}{\hbar\omega_1 - \epsilon_{ml} + i\Gamma} \right), \quad (25a)$$

$$\sigma_{\lambda\alpha\beta}^{(2,ie)}(\omega_1,\omega_2)$$

$$\equiv \sigma_2 g \frac{\hbar^2 \gamma_0}{\Omega a} \sum_{\mathbf{k}} \sum_{mn} \frac{-\bar{\delta}_{mn}\, v_{nm}^{\lambda}}{\hbar(\omega_2+\omega_1) - \epsilon_{mn} + 2i\Gamma}$$

$$\times \left(\frac{v_{mn}^{\alpha} f_{nm}/\epsilon_{mn}}{\hbar\omega_1 - \epsilon_{mn} + i\Gamma} \right)_{;k_{\beta}}, \quad (25b)$$

$$\sigma_{\lambda\alpha\beta}^{(2,ei)}(\omega_1,\omega_2)$$

$$\equiv \sigma_2 g \frac{\hbar^2 \gamma_0}{\Omega a} \sum_{\mathbf{k}} \sum_{mn} \frac{-\bar{\delta}_{mn}/\epsilon_{mn}}{\hbar(\omega_2+\omega_1) - \epsilon_{mn} + 2i\Gamma}$$

$$\times \frac{v_{nm}^{\lambda} v_{mn}^{\beta}}{\hbar\omega_1 + i\Gamma} \frac{\partial f_{nm}}{\partial k_{\alpha}}, \quad (25c)$$

$$\sigma_{\lambda\alpha\beta}^{(2,ii)}(\omega_1,\omega_2)$$

$$\equiv \sigma_2 g \frac{\hbar\gamma_0}{\Omega a} \frac{(\hbar\omega_1 + i\Gamma)^{-1}}{\hbar(\omega_2+\omega_1) - \epsilon_{mn} + 2i\Gamma}$$

$$\times \sum_{\mathbf{k}} \sum_{n} v_{nn}^{\lambda} \frac{\partial^2 f_n}{\partial k_{\beta} \partial k_{\alpha}}. \quad (25d)$$

In these expressions, *ee* refers to a contribution including *interband* matrix elements only, *ii* to that including purely *intraband*, and *ie*, *ei* to those that include one *interband* and one *intraband* matrix element. For later convenience, the constant $\sigma_2 \equiv e^3 a/4\gamma_0\hbar$ is defined in terms of the in-plane nearest-neighbor lattice parameter a and hopping integral γ_0 (cf. Fig. 2). The results (24) completely describe the quadratic response of the system for any combination of the pair of
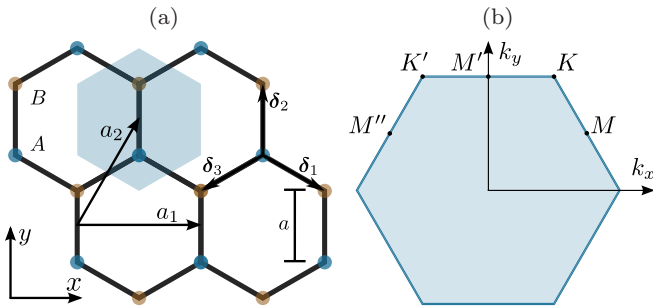

FIG. 2. The 2D honeycomb lattice and respective first Brillouin zone (BZ). The real lattice (a) contains two distinct elements (light and dark disks) and the respective Wigner-Seitz (WS) cell is represented by the shaded hexagon. In (b) we draw the conventional representation of the associated BZ.
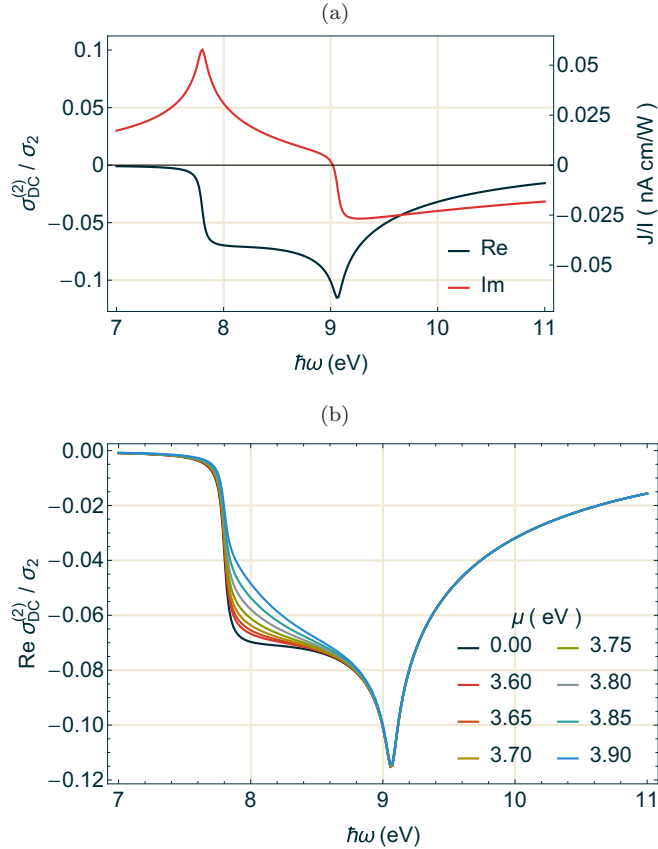
frequencies ω_1 and ω_2. Henceforth, we shall be interested only in the specific case of $\sigma_{222}^{(2)}(\omega,-\omega)$ that characterizes the intrinsic photoconductivity of the system: how much current density is driven in the system for a given intensity and polarization of the incident electromagnetic radiation. This response function is associated with the effect known as photoconductivity. To ease the notation, we define

$$\sigma_{\text{dc}}^{(2)}(\omega) \equiv \sigma_{222}^{(2)}(\omega,-\omega), \quad (26)$$

where the subscript "dc" emphasizes that the induced current is constant in time. Since there is no risk of ambiguity and, moreover, a system with C_3 point-group symmetry has only one independent tensor component, $\sigma_{\text{dc}}^{(2)}(\omega)$ will be used from this point on.

IV. PHOTOCONDUCTIVITY OF MONOLAYER HONEYCOMB LATTICES

To actually compute the linear and quadratic conductivities in Eq. (22) or (24), we must determine not only the electronic energy bands, but also the matrix elements of the velocity $\boldsymbol{v}_{mn}$ and Berry connection $\mathcal{A}_{mn}$ involving any two bands. A simple one-orbital tight-binding (TB) model provides an accurate, yet simple, description of such quantities in graphene and boron nitride (monolayers and bilayers).

Consider the general case of a single layer of a honeycomb lattice where the atoms residing in the A and B sublattices can be different, a canonical example being a monolayer of hBN. The direct and reciprocal lattices of such a crystal are illustrated in Fig. 2. In a single orbital, nearest-neighbor tight-binding modeling of the relevant electronic degrees of freedom, the Hamiltonian operator takes the form

$$\hat{H} = -\gamma_0 \sum_{\mathbf{k}} \Psi_{\mathbf{k}}^{\dagger} h_{\mathbf{k}} \Psi_{\mathbf{k}}, \quad (27)$$

where $\Psi^{\dagger} \equiv [a_{\mathbf{k}}^{\dagger}\ b_{\mathbf{k}}^{\dagger}]$ comprises the Fourier-transformed electron creation operators at sites of the A and B sublattices, and $h_{\mathbf{k}}$ is the reduced Hamiltonian in the crystal momentum representation:

$$h_{\mathbf{k}} \equiv \begin{pmatrix} -\Delta/2 & \phi(\mathbf{k}) \\ \phi^*(\mathbf{k}) & +\Delta/2 \end{pmatrix}. \quad (28)$$

Henceforth, we use units of energy such that $\gamma_0 = 1$. Here, Δ quantifies the difference in the atomic energy of A- and B-type atoms, and $\phi(\mathbf{k}) \equiv e^{ik_y a} + 2e^{-ik_y a/2}\cos(\sqrt{3}k_x a/2)$, a being the nearest-neighbor distance. This description yields the simple two-band energy dispersion

$$\epsilon_{\pm}(\mathbf{k}) = \pm\sqrt{|\phi(\mathbf{k})|^2 + \Delta^2/4}. \quad (29)$$

In this tight-binding parametrization, the velocity matrix elements and Berry connection (28) are simply

$$\hbar\boldsymbol{v}_{mn} = \langle m\mathbf{k}|\nabla_{\mathbf{k}}h_{\mathbf{k}}|m\mathbf{k}\rangle, \quad \mathcal{A}_{mn} = i\langle m\mathbf{k}|\nabla_{\mathbf{k}}|n\mathbf{k}\rangle, \quad (30)$$

where $|n\mathbf{k}\rangle$ are the normalized eigenstates of (28).

A. Hexagonal boron nitride

A system to which the Hamiltonian above is directly relevant is that of a monolayer of boron nitride, whose

FIG. 3. The photoconductivity $\sigma_{\text{dc}}^{(2)}(\omega)$ for a hBN monolayer in units of $\sigma_2 = 3.79 \times 10^{-15}$ S m/V. We consider the TB model (28) ($\gamma_0 = 2.33$ eV, $\Delta = 7.8$ eV, $\Gamma = 0.03$ eV, $\mu = 0$ eV). (a) Real and imaginary parts of $\sigma_{\text{dc}}^{(2)}(\omega)$ at room temperature. Right scale measures the electric current per laser intensity (J/I) [26]. In (b), we analyze the effect of finite doping by showing Re $\sigma_{\text{dc}}^{(2)}(\omega)$ at different chemical potential and high temperature: $T = 1500$ K.

crystal lattice consists of a honeycomb structure where the B and N atoms occupy distinct sublattices. We follow the parametrization of Ref. [14] for the hopping and gap, namely, $\gamma_0 = 2.33$ eV, $\Delta = 7.80$ eV, and the nearest-neighbor distance is $a = 1.45 \times 10^{-10}$ m.

The symmetry constraints greatly facilitate the calculation of the quadratic conductivity because, as only $\sigma_{222}^{(2)}(\omega, -\omega)$ needs to be computed explicitly, the last two contributions (25c) and (25d) vanish identically as long as time-reversal symmetry is preserved. Hence, quite generically only $\sigma_{222}^{(2,ee)}(\omega, -\omega)$ and $\sigma_{222}^{(2,ie)}(\omega, -\omega)$ need to be computed in a system with threefold plane rotational symmetry. Moreover, in any two-band model, $\sigma_{222}^{(2,ee)}$ is also identically zero for the same reason.

Figure 3(a) shows the real and imaginary parts of $\sigma_{\text{dc}}^{(2)}(\omega)$ for a hBN monolayer computed directly from the results in Eq. (24). As anticipated from the nature of the frequency denominators in those expressions, the system mainly responds for photon energies at, or above, the band gap. The peak at ≈ 9 eV is associated with virtual transitions between the van Hove singularities at the M point in the Brillouin zone.

Unlike other two-dimensional (2D) crystals such as graphene or transition-metal dichalcogenides, the large gap in hBN makes it impossible to change the Fermi level by electrostatic gating. On the other hand, a small amount of impurities might introduce a shallow donor (acceptor) band and allow the chemical potential to be driven close to the edge of the conduction (valence) band. This scenario is explored in Fig. 3(b), where we show the effect of varying the chemical potential in the vicinity of the band edge at high temperature. High temperature is chosen here because the interaction with very intense laser light, as required to observe nonlinear effects, generates hot carriers in the material. Experiments [27–32] in graphene indicate hot carrier temperatures in the range 1000 to 3600 K.

B. Gapped graphene

The case of hBN can be seen as an extreme limit of "gapped graphene" in the framework of the effective two-band tight-binding model introduced in (28). We use the designation "gapped graphene" to describe a nearest-neighbor tight-binding model like that of graphene, but where the sublattice symmetry is explicitly broken by introducing a potential energy that differs by an amount Δ between the two sublattices [see (28)]. Second-order nonlinearities are not expected in pristine graphene, or any odd numbered Bernal stacked multilayers due to the presence of an inversion center [33]. Breaking the sublattice symmetry in a monolayer, in addition to opening a band gap, lifts this restriction. It is of general interest to describe and understand the behavior of the photoconductivity as a function of gap magnitude in such a system: on the one hand, such sublattice symmetry breaking has been predicted to take place when graphene is grown or transferred to particular substrates [34–43]; on the other hand, models such as (28) are frequently used as minimal descriptions of the low-energy details in many transition-metal dichalcogenides. We note that inversion symmetry in graphene can also be broken by rolling the material into chiral nanotubes [44], for which the gapped graphene model may also be applied.

Using the parameters relevant for graphene to be definite, we computed explicitly the four nonvanishing elements of the photoconductivity tensor $\sigma_{\lambda\alpha\beta}^{(2)}(\omega, -\omega)$, which are shown in Fig. 4 when the gap $\Delta = 200$ meV. That the curves for distinct components coincide and cannot be distinguished in the figure documents a correct implementation of our computation of the various terms in (24).

The real part of $\sigma_{\text{dc}}^{(2)}(\omega)$ should share key features of the joint density of states for transitions between the valence and conduction bands. In particular, it should display an onset of response at precisely $\hbar\omega = \Delta$ (for $T = 0$), and van Hove singularities at frequencies coinciding with transitions between locally flat portions of the band dispersion. The band-gap feature can be clearly identified in the figure. Note, however, an important difference in contrast to the case shown in Fig. 3 for an actual realization of hBN: for small gap, the response is *much stronger* at frequencies in the vicinity of the gap [compare the magnitude of Re $\sigma_{\text{dc}}^{(2)}(\omega)$ at $\hbar\omega = \Delta$ in the two cases]. Since the low-frequency features are governed by the nature of virtual transitions in the vicinity of the K point of
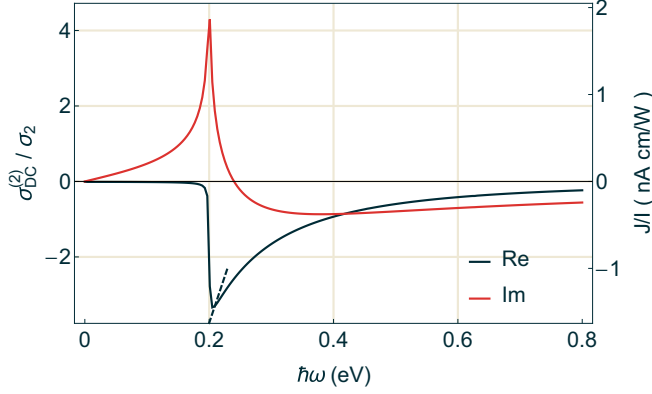
FIG. 4. Real and imaginary parts of the nonvanishing components of the photoconductivity tensor $\sigma_{dc}^{(2)}(\omega)$, $-\sigma_{211}^{(2)}$, $-\sigma_{121}^{(2)}$, and $-\sigma_{112}^{(2)}$, whose curves perfectly overlap as expected from symmetry. Right scale measures the electric current per laser intensity (J/I) [26]. We consider the TB model (28) ($\gamma_0 = 3\,\text{eV}$, $\Delta = 0.2\,\text{eV}$, $\Gamma = 1\,\text{meV}$, $\mu = 0\,\text{eV}$, $T = 1\,\text{K}$).

the Brillouin zone (BZ), we can understand this behavior from an exact analytical standpoint which is possible to establish after expanding (24) in the vicinity of K:

$$\text{Re}\,\sigma_{dc}^{(2)}(\omega) \approx \sigma_2 \left[-\frac{1}{4\Delta} + \left(\frac{21}{32\Delta^2} - \frac{25}{576} \right)(\hbar\omega - \Delta) \right]$$
$$\times \theta(\hbar\omega - \Delta). \qquad (31)$$

This curve that defines the onset of photoconductivity at $\hbar\omega \gtrsim \Delta$ is shown in Figs. 4 and 5(a) as dashed lines.

It is clear that the singular behavior at $\hbar\omega = \Delta$ should be more prominent the smaller the gap. Since the magnitude of $\text{Re}\,\sigma^{(2)}$ there is exactly $-\sigma_2/4\Delta$, the frequencies near the optical absorption edge will entirely dominate the photoconductivity response for gaps smaller than 1 eV. This is shown explicitly in Fig. 5(a), where we plot the photoconductivity for different gaps at very low temperature. The effect of varying the chemical potential is studied in Fig. 5(b) for representative cases. Since all the virtual transitions that define the response in a translationally invariant system are vertical (i.e., conserving the crystal momentum $\mathbf{k}$), at $T \approx 0$ a chemical potential in the conduction band will block any response for $\hbar\omega < 2|\mu|$ due to Pauli exclusion, as seen in the figure.

V. PHOTOCONDUCTIVITY OF BILAYER HONEYCOMB LATTICES

A. Biased bilayer graphene

If it is not clear within the current experimental landscape whether a realization of small Δ gapped graphene is a realistic prospect, the existence of a band gap in biased bilayer graphene (BBG) is a well-established experimental fact [8]. Crucially, its gap is a function of the externally driven interlayer bias voltage and, hence, tunable [8,9]. From this perspective, a BBG is a more natural candidate to explore the quadratic response to light.

A minimal tight-binding model that captures the electronic structure of Bernal-stacked bilayer graphene in the presence of a uniform electric field perpendicular to the plane, is given
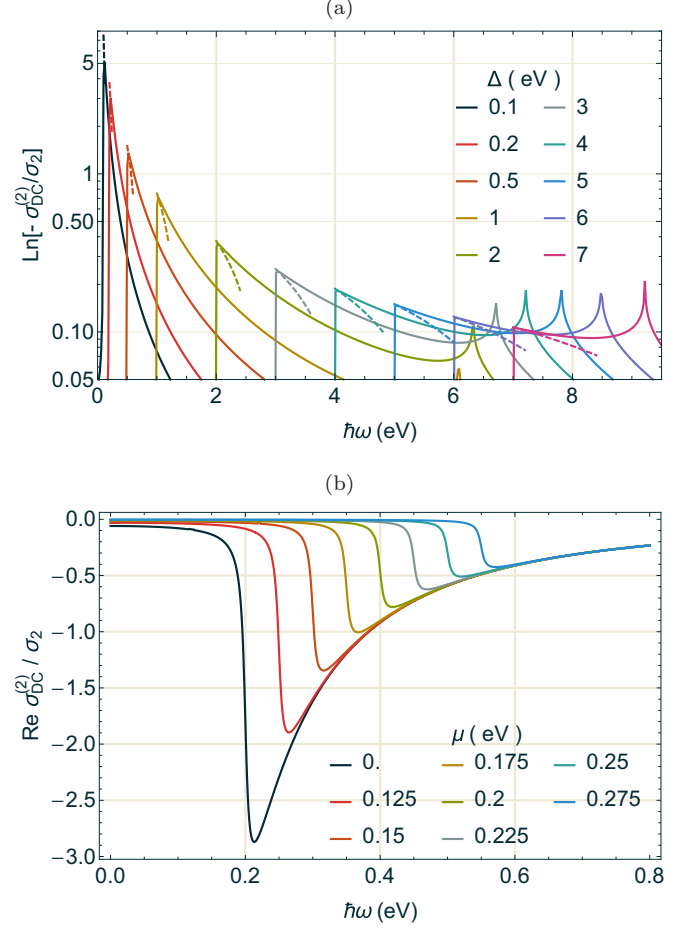

FIG. 5. Photocurrent of gapped graphene as a function of gap (a) and chemical potential (b) whose respective magnitudes are indicated in the legends. In (a), dashed lines refer to the threshold behavior given in Eq. (31), and the vertical scale is logarithmic. Other parameters are as in Fig. 4.

by [9,45]

$$h_{\mathbf{k}}^{\text{BBG}} = \begin{pmatrix} \Delta/2 & \phi(\mathbf{k}) & \gamma_1 & 0 \\ \phi^*(\mathbf{k}) & \Delta/2 & 0 & 0 \\ \gamma_1 & 0 & -\Delta/2 & \phi^*(\mathbf{k}) \\ 0 & 0 & \phi(\mathbf{k}) & -\Delta/2 \end{pmatrix}, \qquad (32)$$

where γ_1 represents the interlayer hopping and Δ the difference in potential energy in the two layers induced by the external field. The dispersion function $\phi(\mathbf{k})$ is the same that appears in Eq. (29). The Hamiltonian (32) is represented in the basis $\{A_1, B_1, B_2, A_2\}$.

The largest gaps obtained by field effect with top- and bottom-gated devices have not so far exceeded 0.5 eV [9,46–50]. Hence, to be specific, we shall analyze the photocurrent in BBG with $\Delta = 200$ meV in the parametrization of (24).

The band structure of BBG can accommodate different types of vertical transitions in the low-energy regime, thereby increasing the richness of the interaction with light. Having now one pair of conduction and another of valence bands means that transitions such as $\epsilon_3 \leftrightarrow \epsilon_1$ or $\epsilon_2 \leftrightarrow \epsilon_4$ become important at low frequencies because the separation between these bands (set by the interlayer hopping γ_1) can easily be
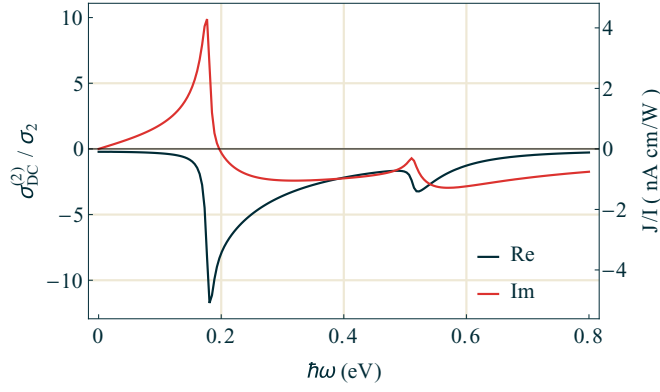
FIG. 6. Photoconductivity of BBG at charge neutrality in units of $\sigma_2 = 2.88 \times 10^{-15}$ S m/V. Right scale measures the electric current per laser intensity (J/I) [26]. We consider the TB model (32) ($\gamma_0 = 3$ eV, $\gamma_1 = 0.4$ eV, $\Delta = 0.2$ eV, $\Gamma = 5$ meV, $\mu = 0$ eV).

comparable to the bias-induced band gap. What is more, chemical potential and bias (hence gap) can be controlled independently in experiments, allowing for a selective suppression of different types of transitions.

Figure 6 shows the intrinsic photoconductivity expected in charge-neutral BBG. At low temperature, the response exhibits two key features associated with the onset of the virtual transitions $\epsilon_1 \leftrightarrow \epsilon_2$ and $\epsilon_1 \leftrightarrow \epsilon_4$ (see Fig. 7 for details of the band labeling). As expected, no features appear related to transitions involving bands $\epsilon_3 \leftrightarrow \epsilon_1$ or $\epsilon_2 \leftrightarrow \epsilon_4$ due to Pauli blocking.

B. Finite temperatures, doping, and broadening

If the temperature is high enough, we can see in Fig. 8(a) that the frequency response becomes much richer, and $\sigma_{dc}^{(2)}(\omega)$ can even change sign in the range $0.3 \lesssim \hbar\omega \lesssim 0.5$ that is dictated by the magnitude of the interlayer hopping γ_1. This is caused by the suppression of Pauli blocking with increasing temperature, leading to the emergence of spectral features
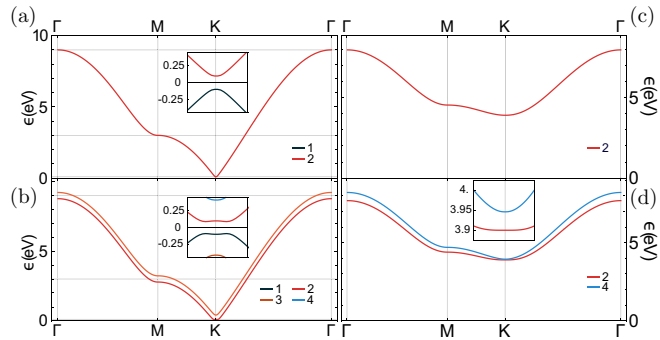

FIG. 7. Conduction band structures along the high-symmetry path $\mathbf{\Gamma} \rightarrow \mathbf{M} \rightarrow \mathbf{K} \rightarrow \mathbf{\Gamma}$ using a TB Hamiltonian (given that all systems under consideration have particle-hole symmetry, we only display the conduction bands). (a) Monolayer graphene ($\gamma_0 = 3$ eV, $\Delta = 0.2$ eV). (b) BBG ($\gamma_0 = 3$ eV, $\gamma_1 = 0.4$ eV, $\Delta = 0.2$ eV). (c) Monolayer hBN ($\gamma_0 = 2.33$ eV, $\Delta = 7.8$ eV). (d) Bilayer AB hBN ($\gamma_0 = 2.33$ eV, $\gamma_1 = 0.6$ eV, $\Delta = 7.8$ eV). Insets in (b) and (d) show the band structure in the vicinity of the K point.
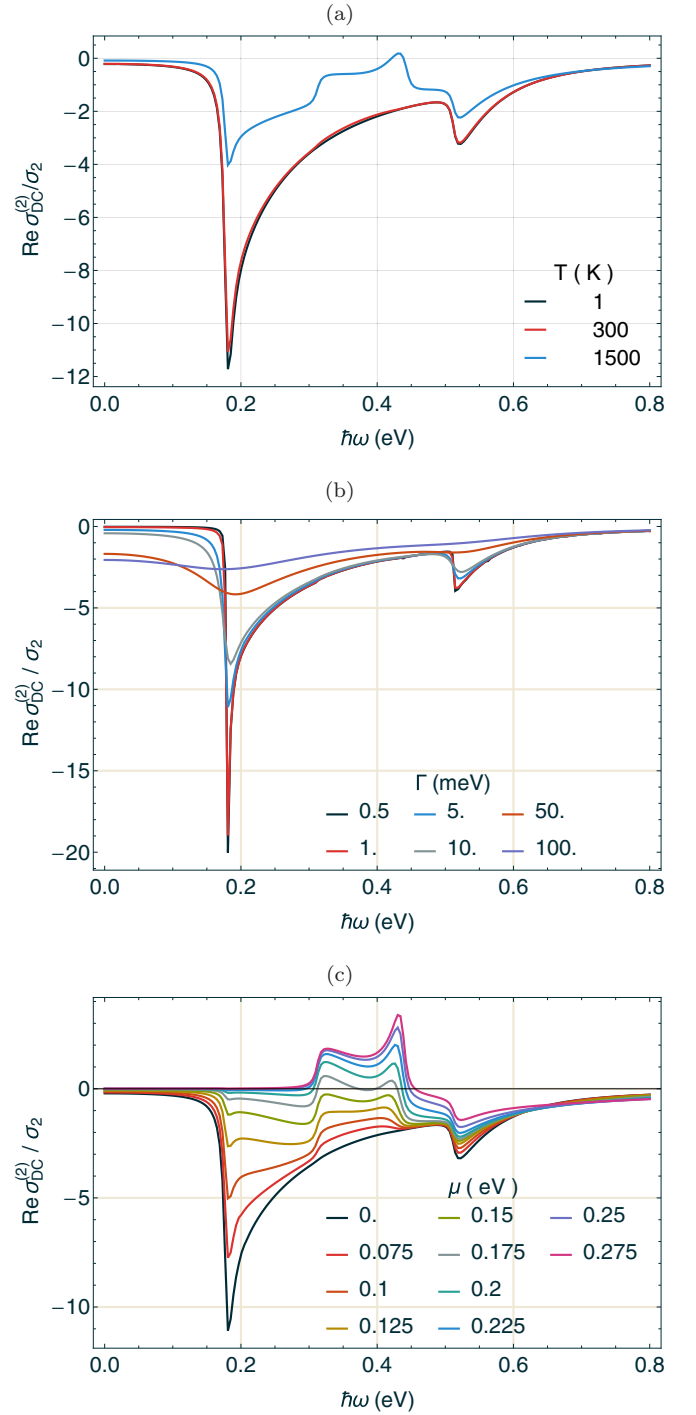

FIG. 8. Photoconductivity of BBG at charge neutrality in units of $\sigma_2 = 2.88 \times 10^{-15}$ S m/V. In (a) we plot the variation of the photoconductivity with temperature. Panels (b) and (c) are calculated at $T = 300$ K and show, respectively, the dependence on the broadening parameter Γ (meV) and chemical potential μ. Other parameters are as in Fig. 6.

associated with transitions from the bands $\epsilon_3 \leftrightarrow \epsilon_1$ and $\epsilon_2 \leftrightarrow \epsilon_4$ that are not effectively possible at room temperature. It is easy to conceive a direct application of this characteristic: since experiments that probe the nonlinear response must be frequently done under relatively high power, the observation

of spectral features expected to be Pauli blocked could be used as an indirect thermometer to estimate the local temperature of the electron gas in the system under illumination.

Since in this paper we are concerned with the generation of a dc electrical current through optical means, it is natural to wonder what effect the scattering of charge carriers by impurities might have in the strength and nature of the photocurrents. Although we do not explicitly include disorder in our calculations, and to the best of our knowledge, disorder has not been addressed in microscopic calculations of the nonlinear optical response, we can draw insight from the effects that weak disorder has in the linear optical conductivity. In this context, several types of disorder have been studied and, in addition to the fact that dilute scatterers lead to perturbations proportional to their concentration, the leading qualitative effect of both short-ranged and Coulomb impurities is the broadening/smearing of the line shape characteristic of the pristine crystals [51–55]. Correspondingly, we expect the main effect of weak disorder in the nonlinear response to be captured qualitatively by making the adiabatic parameter Γ in our calculations explicitly finite, with a magnitude that reflects a phenomenological scattering rate. That would be equivalent to assuming that self-energy corrections arising from disorder are featureless in momentum and frequency, which is a reasonable approximation for these cases. As an illustration, in Fig. 8(b) we study the sensitivity of the photocurrent to that scattering rate for the BBG at room temperature. The main features remain identifiable up to $\Gamma \gtrsim 50$ meV.

Notwithstanding the impact that disorder might have in the dc currents generated by the photogalvanic effect, the continuous progress in the production of high-quality samples, such as encapsulating graphene between hBN crystals [56–59] and other techniques [60], has delivered procedures to achieve graphene-based electronic devices of progressively higher mobility and mean-free paths up to $\ell_f \sim 23\,\mu m$ [58]. This corresponds to a typical lifetime for ballistic transport of $\tau = \ell_f/v_F \sim 2.3$ ps or a scattering rate $\Gamma \sim \hbar/2\Delta t = 0.14$ meV. According to the data in Fig. 8(b), this means that, even though effects such as photon drag might compete with the photogalvanic effect at the quadratic order, it is not unrealistic to anticipate a class of systems where contributions to the photocurrent arising from impurity-assisted processes are minimal, and it is mostly determined by the intrinsic photogalvanic effect discussed here.

Finally, the results presented in Fig. 8(c) at different μ demonstrate that the ability to experimentally vary the chemical potential on demand through simple gating might allow external control over the polarity of the induced photocurrents within target frequency ranges. The sign of $\sigma_{dc}^{(2)}(\omega)$ directly translates into the sign of the dc current in the material and, as we can see in this figure, the photocurrent can be made to switch from positive to negative at frequencies that are controlled by μ.

C. Bilayer boron nitride

As discussed earlier, several types of hBN bilayers can arise from distinct stacking arrangements, but only two are noncentrosymmetric (cf. Table I) and thus relevant in the context of quadratic response. We will consider the AB bilayer
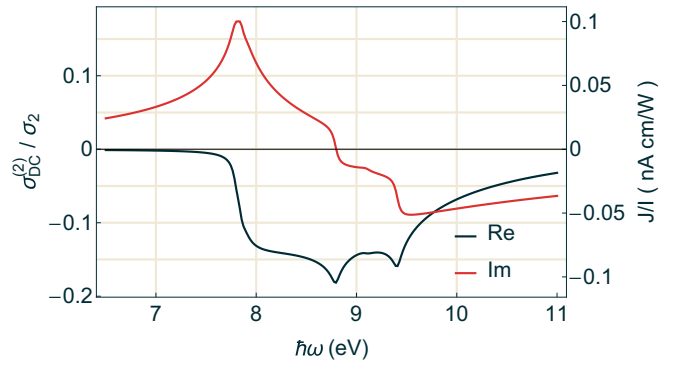

FIG. 9. Photoconductivity of an AB-hBN bilayer in units of $\sigma_2 = 3.79 \times 10^{-15}$ S m/V. Right scale measures the electric current per laser intensity (J/I) [26]. We consider the TB model (33) ($\gamma_0 = 2.33$ eV, $\gamma_1 = 0.6$ eV, $\Delta = 7.8$ eV, $\Gamma = 0.03$ eV, $\mu = 0$ eV, $T = 1$ K).

in the following discussion, which is the counterpart of the Bernal graphene bilayer that results when two superimposed hBN monolayers are displaced so that the N atom (A_1) lies above the B (B_2) in the layer underneath. The corresponding Hamiltonian in the basis $\{A_1, B_1, B_2, A_2\}$ is

$$h_{\mathbf{k}}^{AB} = \begin{pmatrix} -\Delta/2 & \phi(\mathbf{k}) & \gamma_1 & 0 \\ \phi^*(\mathbf{k}) & \Delta/2 & 0 & 0 \\ \gamma_1 & 0 & \Delta/2 & \phi^*(\mathbf{k}) \\ 0 & 0 & \phi(\mathbf{k}) & -\Delta/2 \end{pmatrix}, \quad (33)$$

where, analogously to Eq. (32), Δ is the interlayer bias parameter and γ_1 the interlayer hopping. For consistency with the calculations done earlier in the monolayer, we consider the same in-plane tight-binding parameters $\gamma_0 = 2.33$ eV, $\Delta = 7.80$ eV, and $a = 1.45 \times 10^{-10}$ m. In Ref. [16], a fit to a first-principles calculation of the band structure of AB-BN finds $\gamma_1 = 0.60$ eV and we use this value. Although a finite interlayer bias voltage can be added similarly to BBG and is expected to modify the gap [61], we consider only unbiased hBN bilayers ($\Delta = 0$).

Figure 9 displays the resulting photoconductivity at low temperature for an undoped ($\mu = 0$) hBN bilayer. Since Δ is by far the largest energy scale in hBN, it is no surprise that the shape of $\sigma_{dc}^{(2)}(\omega)$ seen here is almost entirely similar to that of the monolayer (cf. Fig. 3), except for a factor of 2 enhancement in the case of the bilayer on account of the system now having twice as many layers. The one noticeable difference appears associated with the van Hove singularities at the M points of the BZ because, at these saddle points in the energy dispersion, the separation of the pair of valence (and conduction) bands is large (≈ 307 meV), leading to a sizable separation (≈ 614 meV) of the two possible vertical transitions.

An interesting scenario is possible if the bilayer is slightly doped (possibly intentionally by impurities) in order to place the chemical potential at or slightly above the bottom of the lowest conduction band (the same happens if μ is slightly below the top of the highest valence band in a slightly hole-doped scenario) [62,63]. Consider the results shown in Fig. 10(a). At the K point the separation between bands 2
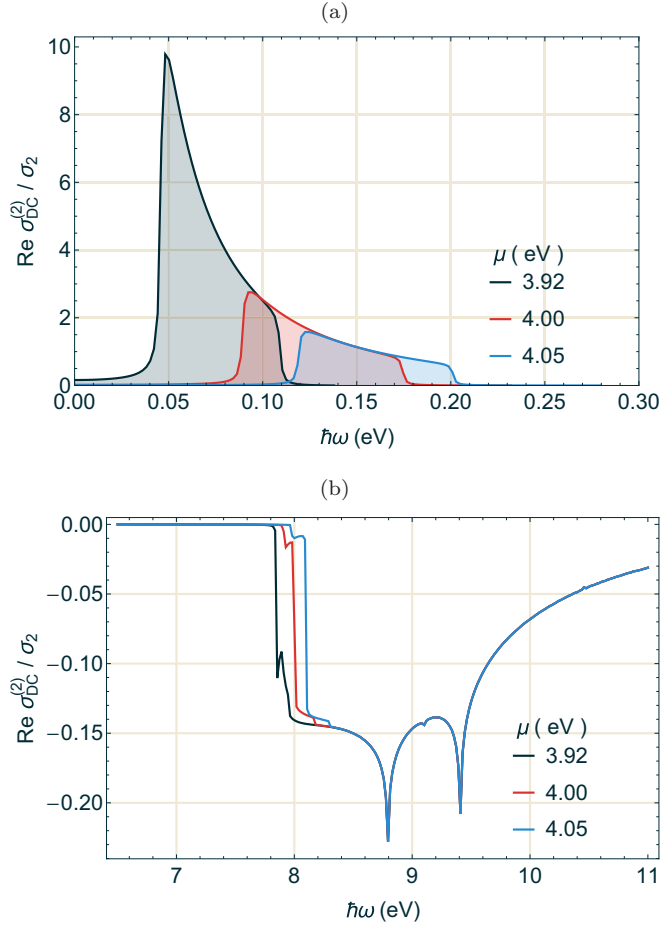
(a)

(b)

FIG. 10. Real part of $\sigma_{\mathrm{dc}}^{(2)}(\omega)$ in a bilayer of AB-stacked hBN at finite doping and $T = 1\,\mathrm{K}$. Only the low-frequency range is shown in panel (a), while (b) displays the high-frequency response. All frequencies in-between show zero $\mathrm{Re}\,\sigma_{\mathrm{dc}}^{(2)}(\omega)$. Note that the energy range in (a) is much smaller than in (b). Other parameters are as in Fig. 9.

and 4 [cf. Fig. 7(d)] is

$$\epsilon_{42} = \frac{\Delta}{2}\left(\sqrt{1 + \frac{4\gamma^2}{\Delta^2}} - 1\right) \approx \gamma_1^2/\Delta = 46\,\mathrm{meV}. \quad (34)$$

Since $\gamma_1/\Delta \ll 1$ in hBN, this separation is rather small when compared with $\epsilon_2 - \epsilon_1 \approx \epsilon_4 - \epsilon_1 \approx \Delta$ to leading order in the gap. As a result, transitions between bands $\epsilon_2 \leftrightarrow \epsilon_4$ open a channel for second-order response at a very low energy ($\sim\gamma_1^2/\Delta$) when compared with typical valence-conduction transitions. Consequently, when hBN is slightly electron doped so that μ straddles the bottom of the two conduction bands one obtains (i) a strong response at frequencies $\hbar\omega \approx 46\,\mathrm{meV}$ that can easily be an order of magnitude higher than the response characteristic of the valence-conduction transitions; (ii) an inversion of the sign of the induced current for low stimulating frequencies in comparison with that for frequencies above the fundamental band gap. The high intensity seen in the low frequency window shown in Fig. 10(a) stems from the fact that these processes arise from interband transitions between bands having approximately the same curvature [see Fig. 7(d)]. As a result, there is a much larger underlying joint density of states

than at higher energies, where the transitions always connect states in bands with opposite curvature. The frequency band showing strong infrared response is controlled by the position of the chemical potential, suggesting that the effect can be manipulated by tailoring the doping level.

VI. ROLE OF EXCITONS IN hBN

Excitons are not a crucial element in elementary descriptions of the optical response of graphene. Even though they do lead to quantitative changes in the position of the van Hove singularities [64] and, therefore, should be properly accounted for in quantitative comparisons with experimental data [65,66], their presence does not introduce significant *qualitative* changes to the frequency dependence of the response functions [65]. In particular, the low-frequency behavior is not visibly sensitive to the inclusion of excitonic corrections due mostly to the fact that graphene has no band gap. In BBG, the band gap allows for the absorption spectrum to be modified in the gap region due to excitons, but the screening from substrates is enough to make these corrections relatively small in comparison with a single-particle description [67].

Boron nitride is different. First-principles calculations indicate that the linear optical conductivity of hBN is strongly renormalized by excitonic corrections [68]. This, although a fact common to all two-dimensional insulator crystals on account of the reduced screening of Coulomb interactions, leads to a particularly strong correction in hBN because of its very large band gap. The second-harmonic susceptibility of hBN studied in Ref. [14] is entirely dominated by the two-particle spectrum and we expect the photoconductivity $\sigma_{\mathrm{dc}}^{(2)}(\omega)$ to be likewise strongly modified.

To that end, we have applied the two-band model [14] of the second-order intraband response to the nonlinear photoconductivity in hBN. The band structure is based on the parameters applied above, i.e., $\gamma_0 = 2.33\,\mathrm{eV}$, $\Delta = 7.8\,\mathrm{eV}$ and screening is implemented as in Ref. [14]. The resulting exciton spectrum is shown in Fig. 11, which should be contrasted with the independent-electron result in Fig. 3(a). For a direct comparison, the latter is reproduced as the shaded curves in Fig. 11. It is apparent that Coulomb effects cause a marked
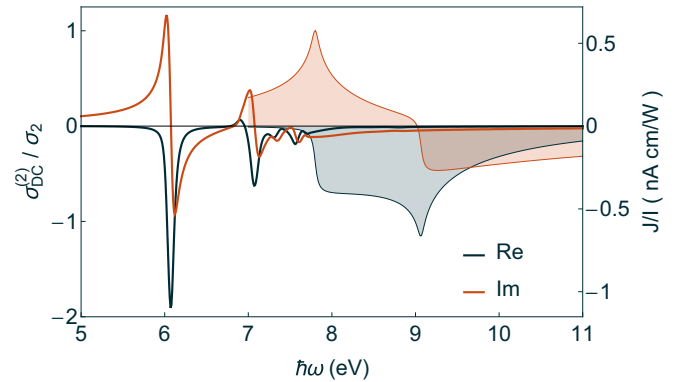

FIG. 11. Photoconductivity of a hBN monolayer with excitonic corrections. Model parameters are identical to those in Fig. 3. The shadowed curves reproduce the independent-particle results shown in Fig. 3, vertically scaled up by a factor of 10.

red-shift by nearly 2 eV of the onset of the photoconductive response: the prominent band-gap feature characteristic of the independent-electron response at 7.8 eV is down-shifted to the fundamental exciton energy around 6.1 eV. It is also noted that the magnitude of the response at frequencies associated with well-isolated exciton levels is dramatically increased (in excess of tenfold) in comparison with the noninteracting case. At the same time, whereas the curve of $\sigma_{dc}^{(2)}(\omega)$ is markedly structured in the frequency range containing well-defined excitons, it becomes quite featureless above the noninteracting band gap. This is a consequence of the large spectral weight carried by the excitonic peaks that implies a depletion in the response at frequencies above the band gap. This is analogous to the behavior observed in the (linear) optical absorption spectrum of this material [68]. The colossal excitonic effects derive mainly from the poor screening in large-gap two-dimensional insulators, of which hBN is clearly an extreme case. In view of the close similarity between the photoconductivity of hBN monolayers and bilayers seen at the independent-particle level [cf. Figs. 3(a) and 9], we expect an equally strong renormalization of the response in the undoped bilayers. In general, less pronounced modifications are expected for low-gap systems such as bilayer graphene or other realizations of the more general "gapped graphene" model discussed above, as well as in the lightly doped scenarios discussed before.

VII. CONCLUSION

The photoconductivity provides a direct measure of the ability to directly inject dc currents in a system by purely optical means. Harnessing and being able to tailor this effect can lead to improved optoelectronic device concepts and functionalities. Two-dimensional crystals are excellent materials to explore towards this end due to the intrinsic ease of integration in flat heterostructures, the possibility of controlling the electronic density through field effect, or the ability to modify their electronic structure by various types of surface modification. We have explored the photoconductivity of honeycomb-based electronic systems in monolayer and bilayer form and resorted to the examples of graphene and hBN for a definite illustration of its behavior in the cases of small and large band gap.

Our calculations were done in the length gauge within the framework originally discussed by Sipe and collaborators [11]. In the systems derived from graphene, an independent-particle approach should provide a good qualitative and quantitative characterization of the response. We therefore trust that our

results for BBG are entirely realistic, and similarly for those pertaining to the "gapped graphene" model, provided the gaps are kept small. In particular, our results in Sec. V A show that the ability to independently tune both the gap and density in BBG can lead to a very rich and density-dependent photogalvanic response. On the other hand, those structures based on undoped hBN necessarily require an explicit treatment of the Coulomb interactions between particle-hole pairs. By solving the Bethe-Salpeter equation and computing the resulting photogalvanic response, we have shown in Sec. VI that the reduced screening in two dimensions leads to robust excitons with large binding energies that, not only strongly renormalize the onset of the response to much lower energies, but, importantly, concentrate most of the spectral weight for $\sigma_{dc}^{(2)}(\omega)$. Therefore, similarly to their crucial impact in the absorption spectrum, interaction effects are clearly unavoidable in an accurate model of the photoconductivity for hBN. In a lightly doped scenario, however, the enhanced metallic screening is expected to significantly suppress the Coulomb interaction and bring the system's response closer to that of an independent-particle description. Experiments reporting doping by carbon substitution have been reported in hBN films, nanotubes, and nanoribbons [62,63]. It has also been predicted that intercalation or adsorption with alkali elements can produce shallow donor states with minimal impact in the underlying band structure [69]. In this case, the features discussed in Sec. V C should hold, and one expects a strong photoconductivity in a narrow frequency band in the infrared. The existence and width of this band are controlled by the position of the chemical potential within the two conduction subbands, and suggests the possibility of generating photogalvanic currents in hBN with frequencies much smaller than the fundamental band gap.

[1] M. Bass, P. A. Franken, F. Ward, and G. Weinreich, Phys. Rev. Lett. **9**, 446 (1962).

[2] E. L. Ivchenko, *Optical Spectroscopy of Semiconductor Nanostructures* (Alpha Science, Middlesex, UK, 2005), p. 350.

[3] R. Ghosh and L. Mandel, Phys. Rev. Lett. **59**, 1903 (1987).

[4] Y. H. Shih and C. O. Alley, Phys. Rev. Lett. **61**, 2921 (1988).

[5] R. W. Boyd, *Nonlinear Optics*, 3rd ed. (Elsevier, Amsterdam, 2008).

[6] Y. R. Shen, *The Principles of Nonlinear Optics* (Wiley, Hoboken, NJ, 2003).

[7] S. Haussühl, in *Physical Properties of Crystals*, edited by S. Hausshl (Wiley-VCH, Weinheim, Germany, 2007).

[8] Y. Zhang, V. W. Brar, C. Girit, A. Zettl, and M. F. Crommie, Nat. Phys. **5**, 722 (2009).

[9] E. V. Castro, K. S. Novoselov, S. V. Morozov, N. M. R. Peres, J. M. B. Lopes dos Santos, J. Nilsson, F. Guinea, A. K. Geim, and A. H. Castro Neto, Phys. Rev. Lett. **99**, 216802 (2007).

[10] A. Das, S. Pisana, B. Chakraborty, S. Piscanec, S. K. Saha, U. V. Waghmare, K. S. Novoselov, H. R. Krishnamurthy,

A. K. Geim, A. C. Ferrari, and A. K. Sood, Nat. Nanotechnol. **3**, 210 (2008).

[11] C. Aversa and J. E. Sipe, Phys. Rev. B **52**, 14636 (1995).

[12] S. J. Brun and T. G. Pedersen, Phys. Rev. B **91**, 205405 (2015).

[13] M. L. Trolle, G. Seifert, and T. G. Pedersen, Phys. Rev. B **89**, 235410 (2014).

[14] T. G. Pedersen, Phys. Rev. B **92**, 235432 (2015).

[15] M. S. Dresselhaus, G. Dresselhaus, and A. Jorio, *Group Theory* (Springer, Berlin, 2008).

[16] R. M. Ribeiro and N. M. R. Peres, Phys. Rev. B **83**, 235312 (2011).

[17] J. J. Sakurai, *Advanced Quantum Physics*, 1st ed. (Addison-Wesley, Berlin, 1967).

[18] E. Blount, Solid State Phys. **13**, 305 (1962).

[19] D. J. Moss, E. Ghahramani, J. E. Sipe, and H. M. van Driel, Phys. Rev. B **41**, 1542 (1990).

[20] M. V. Berry, Proc. R. Soc. A **392**, 45 (1984).

[21] D. Xiao, M.-C. Chang, and Q. Niu, Rev. Mod. Phys. **82**, 1959 (2010).

[22] V. P. Gusynin and S. G. Sharapov, Phys. Rev. B **73**, 245411 (2006).

[23] N. M. R. Peres, F. Guinea, and A. H. Castro Neto, Phys. Rev. B **73**, 125411 (2006).

[24] T. Stauber, N. M. R. Peres, and A. K. Geim, Phys. Rev. B **78**, 085432 (2008).

[25] K. F. Mak, M. Y. Sfeir, Y. Wu, C. H. Lui, J. A. Misewich, and T. F. Heinz, Phys. Rev. Lett. **101**, 196405 (2008).

[26] Given a linearly polarized electric field along $\hat{\mathbf{e}}_2$, the photocurrent depends exclusively on the real part of the photoconductivity. Hence, the ratio between the electric current per laser intensity (J/I) to the real part of photoconductivity tensor in units of σ_2 reads as $\frac{J/I}{\mathrm{Re}\,\sigma_{\mathrm{dc}}^{(2)}(\omega)/\sigma_2} = 4 \times 10^{11}\, \sigma_2/n\varepsilon_0 c_0$ nA cm/W, where n is refractive index, ε_0 the vacuum permittivity, and c_0 the speed of light in vacuum. For hBN- or graphene-based systems, the ratios are $\approx\{0.576, 0.434\}$, respectively.

[27] D. Sun, Z.-K. Wu, C. Divin, X. Li, C. Berger, W. A. de Heer, P. N. First, and T. B. Norris, Phys. Rev. Lett. **101**, 157402 (2008).

[28] B. A. Ruzicka, S. Wang, L. K. Werake, B. Weintrub, K. P. Loh, and H. Zhao, Phys. Rev. B **82**, 195414 (2010).

[29] B. A. Ruzicka, L. K. Werake, H. Zhao, S. Wang, and K. P. Loh, Appl. Phys. Lett. **96**, 173106 (2010).

[30] C. H. Lui, K. F. Mak, J. Shan, and T. F. Heinz, Phys. Rev. Lett. **105**, 127404 (2010).

[31] D. Sun, G. Aivazian, A. M. Jones, J. S. Ross, W. Yao, D. Cobden, and X. Xu, Nat. Nanotechnol. **7**, 114 (2012).

[32] K. J. Tielrooij, J. C. W. Song, S. A. Jensen, A. Centeno, A. Pesquera, A. Zurutuza Elorza, M. Bonn, L. S. Levitov, and F. H. L. Koppens, Nat. Phys. **9**, 248 (2013).

[33] A. Jorio, R. Saito, G. Dresselhaus, and M. S. Dresselhaus, *Raman Spectroscopy in Graphene Related Systems* (Wiley-VCH, Weinheim, Germany, 2011).

[34] G. Giovannetti, P. A. Khomyakov, G. Brocks, P. J. Kelly, and J. van den Brink, Phys. Rev. B **76**, 073103 (2007).

[35] S. Y. Zhou, G.-H. Gweon, A. V. Fedorov, P. N. First, W. A. de Heer, D.-H. Lee, F. Guinea, A. H. Castro Neto, and A. Lanzara, Nat. Mater. **6**, 916 (2007).

[36] J. Sławińska, I. Zasada, and Z. Klusek, Phys. Rev. B **81**, 155433 (2010).

[37] C. R. Dean, A. F. Young, I. Meric, C. Lee, L. Wang, S. Sorgenfrei, K. Watanabe, T. Taniguchi, P. Kim, K. L. Shepard, and J. Hone, Nat. Nanotechnol. **5**, 722 (2010).

[38] C. Ortix, L. Yang, and J. van den Brink, Phys. Rev. B **86**, 081405 (2012).

[39] Zhi-Guo Chen, Zhiwen Shi, Wei Yang, Xiaobo Lu, You Lai, Hugen Yan, Feng Wang, Guangyu Zhang, and Zhiqiang Li, Nat. Commun. **5**, 4461 (2014).

[40] M. Bokdam, T. Amlaki, G. Brocks, and P. J. Kelly, Phys. Rev. B **89**, 201404 (2014).

[41] C. R. Woods, L. Britnell, A. Eckmann, R. S. Ma, J. C. Lu, H. M. Guo, X. Lin, G. L. Yu, Y. Cao, R. V. Gorbachev, A. V. Kretinin, J. Park, L. A. Ponomarenko, M. I. Katsnelson, Y. N. Gornostyrev, K. Watanabe, T. Taniguchi, C. Casiraghi, H-J. Gao, A. K. Geim, and K. S. Novoselov, Nat. Phys. **10**, 451 (2014).

[42] M. Yankowitz, J. Xue, and B. J. LeRoy, J. Phys.: Condens. Matter **26**, 303201 (2014).

[43] L. Huang, Q. Yue, J. Kang, Y. Li, and L. Jingbo, J. Phys.: Condens. Matter **26**, 295304 (2014).

[44] T. G. Pedersen and K. Pedersen, Phys. Rev. B **79**, 035422 (2009).

[45] E. McCann and V. I. Fal'ko, Phys. Rev. Lett. **96**, 086805 (2006).

[46] B. N. Szafranek, D. Schall, M. Otto, D. Neumaier, and H. Kurz, Nano Lett. **11**, 2640 (2011).

[47] J. Velasco, L. Jing, W. Bao, Y. Lee, P. Kratz, V. Aji, M. Bockrath, C. N. Lau, C. Varma, R. Stillwell, D. Smirnov, F. Zhang, J. Jung, and A. H. MacDonald, Nat. Nanotechnol. **7**, 156 (2012).

[48] A. Pachoud, M. Jaiswal, P. K. Ang, K. P. Loh, and B. Oezyilmaz, Europhys. Lett. **92**, 27001 (2010).

[49] L. Britnell, R. V. Gorbachev, R. Jalil, B. D. Belle, F. Schedin, A. Mishchenko, T. Georgiou, M. I. Katsnelson, L. Eaves, S. V. Morozov, N. M. R. Peres, J. Leist, A. K. Geim, K. S. Novoselov, and L. A. Ponomarenko, Science **335**, 947 (2012).

[50] A. A. Stabile, A. Ferreira, J. Li, N. M. R. Peres, and J. Zhu, Phys. Rev. B **92**, 121411 (2015).

[51] N. M. R. Peres, T. Stauber, and A. H. Castro Neto, Europhys. Lett. **84**, 38002 (2008).

[52] T. Stauber, N. M. R. Peres, and A. H. Castro Neto, Phys. Rev. B **78**, 085418 (2008).

[53] T. Stauber and N. M. R. Peres, J. Phys.: Condens. Matter **20**, 055002 (2008).

[54] D. S. L. Abergel, H. Min, E. H. Hwang, and S. Das Sarma, Phys. Rev. B **85**, 045411 (2012).

[55] S. Yuan, R. Roldán, H. De Raedt, and M. I. Katsnelson, Phys. Rev. B **84**, 195418 (2011).

[56] W. Gannett, W. Regan, K. Watanabe, T. Taniguchi, M. F. Crommie, and A. Zettl, Appl. Phys. Lett. **98**, 242105 (2011).

[57] T. Chari, I. Meric, C. Dean, and K. Shepard, IEEE Trans. Electron Devices **62**, 4322 (2015).

[58] L. Banszerus, M. Schmitz, S. Engels, M. Goldsche, K. Watanabe, T. Taniguchi, B. Beschoten, and C. Stampfer, Nano Lett. **16**, 1387 (2016).

[59] G. X. Ni, L. Wang, M. D. Goldflam, M. Wagner, Z. Fei, A. S. McLeod, M. K. Liu, F. Keilmann, B. Özyilmaz, A. H. Castro Neto, J. Hone, M. M. Fogler, and D. N. Basov, Nat. Photonics **10**, 244 (2016).

[60] E. Pallecchi, F. Lafont, V. Cavaliere, F. Schopfer, D. Mailly, W. Poirier, and A. Ouerghi, Sci. Rep. **4**, 4558 (2014).

[61] Z. Yang and J. Ni, J. Appl. Phys. **107**, 104301 (2010).

[62] M. Terrones, J. M. Romo-Herrera, E. Cruz-Silva, F. López-Urías, E. Muñoz-Sandoval, J. J. Velázquez-Salazar, H. Terrones, Y. Bando, and D. Golberg, Mater. Today **10**, 30 (2007).

[63] X. Wei, M.-S. Wang, Y. Bando, and D. Golberg, ACS Nano **5**, 2916 (2011).

[64] L. Yang, J. Deslippe, C. H. Park, M. L. Cohen, and S. G. Louie, Phys. Rev. Lett. **103**, 186802 (2009).

[65] V. G. Kravets, A. N. Grigorenko, R. R. Nair, P. Blake, S. Anissimova, K. S. Novoselov, and A. K. Geim, Phys. Rev. B **81**, 155413 (2010).

[66] K. F. Mak, F. H. da Jornada, K. He, J. Deslippe, N. Petrone, J. Hone, J. Shan, S. G. Louie, and T. F. Heinz, Phys. Rev. Lett. **112**, 207401 (2014).

[67] C. H. Park and S. G. Louie, Nano Lett. **10**, 426 (2010).

[68] L. Wirtz, A. Marini, and A. Rubio, Phys. Rev. Lett. **96**, 126104 (2006).

[69] F. Oba, A. Togo, I. Tanaka, K. Watanabe, and T. Taniguchi, Phys. Rev. B **81**, 075125 (2010).